To appear in Proc. ICUAS 2012

Observability-based Optimization of Coordinated Sampling Trajectories for Flowfield Estimation

Levi DeVries, Sharanya J. Majumdar, and Derek A. Paley

Abstract— **Autonomous vehicles are effective environmental sampling platforms whose sampling performance can be optimized by path-planning algorithms that drive vehicles to specific regions of the operational domain containing the most informative data. In this paper, we apply tools from nonlinear observability, nonlinear control, and Bayesian estimation to derive a multi-vehicle control algorithm that steers vehicles to an optimal sampling formation in an estimated flowfield. Sampling trajectories are optimized using the empirical observability gramian. We reconstruct the parameters of the flowfield from noisy flow measurements collected along the sampling trajectories using a recursive Bayesian filter.**

I. INTRODUCTION

An autonomous vehicle sampling in an environment inaccessible to a manned vehicle can shed light on physical processes in the atmosphere and ocean [1],[2],[3]. However, there exists a need to optimize vehicle sampling trajectories such that they provide the most informative data. For example, large-scale severe weather systems such as hurricanes span tens to hundreds of thousands of square kilometers [4], of which even the longest endurance hurricane-sampling vehicle covers just a small fraction. Automatic control algorithms can steer multiple vehicles to coordinated sampling trajectories that are designed for data collection. This paper utilizes tools from nonlinear observability to optimize coordinated sampling trajectories for flowfield estimation. The estimator performance is improved by maximizing the observability of flowfield parameters over a candidate set of coordinated trajectories [5].

This work falls within the general context of (mobile) sensor placement for estimation of an unknown field [6],[7],[8]. The goal is to place a finite number of sensors in a possibly mobile configuration that maximizes an associated cost function. We use the empirical observability gramian [7], [9] to evaluate candidate sampling trajectories and implement a recursive Bayesian filter to estimate an unknown flowfield from noisy measurements collected along the trajectories. The empirical observability gramian has been previously employed for sensor placement in monitoring chemical reactions [7] and for model reduction of high-dimensional nonlinear systems [10]. Related work [6] provides placement strategies for static sensors in order to achieve optimal coverage of a time-invariant field. In distributed parameter estimation [11], [12], and [13], one assumes the unknown field follows a known process model such as a partial differential equation and estimates the unknown parameters associated with the model. An alternate strategy using sensor platforms with time-varying communication is a distributed information-consensus filter [14].

Techniques exist to estimate wind fields using unmanned aircraft. The authors in [15] implemented an unscented Kalman filter to estimate wind disturbances affecting microscale unmanned aerial vehicles. In [16] the authors provide a method for estimating wind fields for small and mini unmanned aerial vehicles. At the macroscale, the authors in [17] implemented an extended Kalman filter to provide wind shear estimates for use in feedback control of aircraft. In [8] the authors used Gaussian process regression to estimate a wind field for exploration and exploitation by

This work is supported by the National Science Foundation under CMMI Grant Nos. CMMI0928416 and CMMI0928198 and the Office of Naval Research under Grant No. N00014-09-1-1058.

Levi DeVries is a graduate student in the Department of Aerospace Engineering at the University of Maryland, College Park, MD 20742 lddevrie@umd.edu

Sharanya J. Majumdar is an associate professor in the Rosenstiel School of Marine and Atmospheric Science at the University of Miami, Miami, FL 33149 smajumdar@rsmas.miami.edu

Derek A. Paley is an assistant professor in the Department of Aerospace Engineering at the University of Maryland, College Park, MD 20742 dpaley@umd.edu

gliding UAV's.

A tool well suited to evaluate the effectiveness of candidate sensor measurements is nonlinear observability. The authors in [9] used the nonlinear observability rank condition [18] to evaluate the effectiveness of Lagrangian drifter sensors for estimating point vortex flows, whereas the authors in [19] assimilated Lagrangian drifter measurements in an extended Kalman filter to estimate ocean flows. In this paper we calculate the empirical observability gramian resulting from measurements collected by each sampling vehicle. The empirical observability gramian is proportional to the Fisher information matrix [20], differing by only the measurement noise covariance. The singular values of the observability gramian provide a measure of flowfield observability along a candidate sampling trajectory. Observability of the flowfield is optimized here by maximizing the smallest singular value of the observability gramian over a set of candidate trajectories, although other metrics exist [7], [20].

We take the following technical approach to design an observability-based sampling algorithm and apply it to sampling an idealized vortex model. We assume the vehicles collect noisy measurements of the flowfield and implement a recursive Bayesian filter to estimate the flowfield parameters. Using the estimated flowfield, we calculate the smallest singular value of the empirical observability gramian to optimize sampling trajectories over a given time interval. The optimal sampling trajectories and the estimated flowfield are then implemented in a decentralized nonlinear, multi-vehicle control algorithm to steer vehicles along optimized sampling trajectories, which in this case are circular formations.

The contributions of this work are (1) a framework to evaluate candidate sampling trajectories in a time-invariant flowfield using flowfield parameter observability as a scoring metric; (2) a decentralized multi-vehicle control to steer vehicles to circular formations that are a specified distance from a reference position, which constitute the set of candidate sampling trajectories; and (3) a multi-vehicle control algorithm using nonlinear observability and recursive Bayesian estimation to reconstruct a time-invariant flowfield from noisy flow measurements. The contributions are illustrated via numerical simulations in a Rankine vortex flow.

Section II describes a self-propelled particle model of vehicles in a moderate flowfield; nonlinear observability measures; and recursive Bayesian estimation. Section III provides a decentralized multi-vehicle control that steers vehicles to circular formations at a specified distance from the origin. In addition, Section III applies nonlinear observability measures to evaluate candidate sampling trajectories in a parameterized flowfield. Section IV presents a multi-vehicle control algorithm for optimal sampling of a parameterized flowfield and provides numerical simulations of the theoretical results. Section V summarizes the paper and describes ongoing research.

II. Control Objective and Background

The general control problem we address here is the optimization of an observer-based feedback controller using observability measures as a design metric. We assume there is a fleet of N sampling vehicles collecting measurements of a known, time-invariant flowfield characterized by M parameters. The vehicles are steered by a decentralized feedback controller parameterized by Q control parameters. The overall system, which may be nonlinear, is[1]

$$\begin{aligned} \dot{\mathbf{z}} &= g(\mathbf{z}, \mathbf{u}(\mathbf{z}, \hat{\mathbf{\Omega}}; \boldsymbol{\chi}); \mathbf{\Omega}) \\ \boldsymbol{\alpha} &= h(\mathbf{z}, \mathbf{u}(\mathbf{z}, \hat{\mathbf{\Omega}}; \boldsymbol{\chi}); \mathbf{\Omega}), \end{aligned} \tag{1}$$

where $\mathbf{z}$ contains the states of all N vehicles. The dynamic control $\mathbf{u}$ is a function of the vehicle states $\mathbf{z}$ augmented by the estimated flowfield parameters $\hat{\mathbf{\Omega}} \in \mathbb{R}^M$ and parameterized by $\boldsymbol{\chi} \in \mathbb{R}^Q$. The function $g(\cdot)$ represents the vehicle dynamics that are affected by the flow and therefore depend on the flowfield parameters $\mathbf{\Omega}$. The outputs $\boldsymbol{\alpha}$ are measurements of the flowfield.

When we assume vehicles collect noisy measurements of the flow, an observer is implemented to provide estimates of the flowfield parameters $\hat{\mathbf{\Omega}}$. The observer dynamics are

$$\dot{\hat{\mathbf{\Omega}}} = w(\mathbf{z}, \hat{\mathbf{\Omega}}, \tilde{\boldsymbol{\alpha}}), \tag{2}$$

[1]The notation $g(a, b; \alpha, \beta)$ represents a function $g(\cdot)$ that depends on the state variables a, b and the parameters α and β. We use bold fonts to represent either a column matrix, e.g., of vehicle positions $\mathbf{r} = [r_1 \ r_2 \ \ldots \ r_N]^T$, or a set of parameters, e.g., $\mathbf{\Omega} = (\Omega_1, \Omega_2, \ldots, \Omega_M)$.

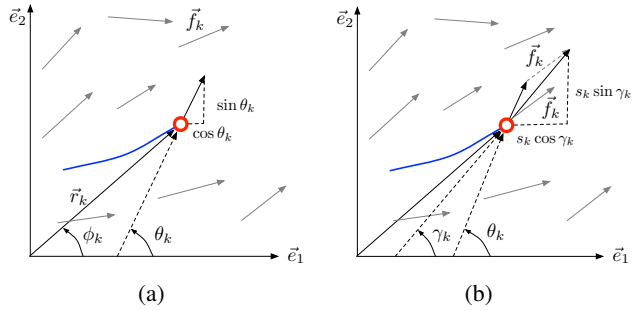

Fig. 1. Model of (a) flow-relative velocity and (b) total velocity.

where $\tilde{\boldsymbol{\alpha}} = \boldsymbol{\alpha} + \boldsymbol{\eta}$ are measurements corrupted by noise $\boldsymbol{\eta}$. In this paper we implement (2) in discrete time using a Bayesian filter. The goal is to optimize the control parameters $\boldsymbol{\chi}$ using the flowfield estimates $\hat{\boldsymbol{\Omega}}$ such that the $\hat{\boldsymbol{\Omega}}$ converges to $\boldsymbol{\Omega}$.

The remainder of this section reviews contributions from prior work that are utilized in Sections III and IV. First, we review a planar model of self-propelled particle motion in a moderate time-invariant flowfield in which the flow magnitude is strictly less than the vehicle speed. Then we define measures of the observability of nonlinear systems. Finally, we describe a framework for recursive Bayesian estimation of a time-invariant flowfield.

A. Vehicle Dynamics in a Moderate Flowfield

This section reviews a two-dimensional model of self-propelled particle motion in a moderate flowfield [21],[22],[23],[24],[25],[26], in which each particle assumes control of its turn rate relative to the flow. Control of the total-velocity turn rate is assumed by utilizing a coordinate transformation [21] that is nonsingular as long as the flow speed does not exceed the vehicle speed.

Consider a collection of N planar Newtonian particles each able to control its turn rate. The k^{th} particle's position with respect to a ground-fixed inertial reference frame $\mathscr{I} = (O, \vec{e}_1, \vec{e}_2)$ is represented by the vector $\vec{r}_k = x_k\vec{e}_1 + y_k\vec{e}_2 \in \mathbb{R}^2$ as shown in Figure 1(a). For $||\vec{r}_k|| \neq 0$ the polar coordinates (r_k, ϕ_k) of the k^{th} particle's position are

$$r_k = \sqrt{x_k^2 + y_k^2} \tag{3}$$

$$\phi_k = \tan^{-1}(y_k/x_k). \tag{4}$$

Each particle's motion is controlled by a gyroscopic steering force normal to its velocity $\dot{\vec{r}}_k = \dot{x}_k\vec{e}_1 + \dot{y}_k\vec{e}_2$. In the absence of flow, $\dot{\vec{r}}_k$ has constant magnitude, which we assume to be unity without loss of generality. The orientation of the k^{th} particle's velocity is a point θ_k on the unit circle, such that $\dot{x}_k = \cos\theta_k$ and $\dot{y}_k = \sin\theta_k$. The decentralized steering control $\dot{\theta}_k = u_k(\mathbf{r}, \boldsymbol{\theta}; \boldsymbol{\chi})$ is designed using state-feedback control when the states are known and observer-based feedback otherwise. The flow-free equations of motion of the k^{th} particle are [22]

$$\begin{aligned} \dot{x}_k &= \cos\theta_k \\ \dot{y}_k &= \sin\theta_k \\ \dot{\theta}_k &= u_k. \end{aligned} \tag{5}$$

Next we augment the model (5) by including a time-invariant, spatially varying flowfield $\vec{f}_k = f_{x,k}\vec{e}_1 + f_{y,k}\vec{e}_2$ whose magnitude is strictly less than one. The flowfield is parameterized by $\boldsymbol{\Omega} \in \mathbb{R}^M$, i.e.,

$$\begin{aligned} f_{x,k} &= f_x(x_k, y_k; \boldsymbol{\Omega}) \in \mathbb{R} \\ f_{y,k} &= f_y(x_k, y_k; \boldsymbol{\Omega}) \in \mathbb{R}. \end{aligned} \tag{6}$$

For example, consider the following Rankine vortex model [9], for which $\boldsymbol{\Omega} = (r_{max}, v_{max}, \mu)$:

$$f_{x,k} = \begin{cases} -v_{max}\,(r_k/r_{max})\sin\phi_k, & 0 < r_k < r_{max} \\ -v_{max}\,(r_k/r_{max})^{-\mu}\sin\phi_k, & r_k > r_{max}, \end{cases} \tag{7}$$

and

$$f_{y,k} = \begin{cases} v_{max}\,(r_k/r_{max})\cos\phi_k, & 0 < r_k < r_{max} \\ v_{max}\,(r_k/r_{max})^{-\mu}\cos\phi_k, & r_k > r_{max}. \end{cases} \tag{8}$$

In the presence of flowfield $\vec{f}_k$, each particle's velocity is represented by the vector sum of its velocity relative to the flow and the flow velocity relative to the ground, as shown in Figure 1(b). The equations of motion of the k^{th} particle become [21], [27]

$$\begin{aligned} \dot{x}_k &= \cos\theta_k + f_{x,k} \\ \dot{y}_k &= \sin\theta_k + f_{y,k} \\ \dot{\theta}_k &= u_k. \end{aligned} \tag{9}$$

For the purpose of path planning in a flowfield, we desire control of the inertial velocity rather than the velocity relative to the flow. For this reason, we define the magnitude and orientation of the total velocity

$$s_k \triangleq \sqrt{\dot{x}_k^2 + \dot{y}_k^2} \tag{10}$$

$$\gamma_k \triangleq \tan^{-1}(\dot{y}_k/\dot{x}_k), \tag{11}$$

such that, from Figure 1(b),

$$s_k \cos\gamma_k = \cos\theta_k + f_{x,k} \quad (12)$$
$$s_k \sin\gamma_k = \sin\theta_k + f_{y,k}. \quad (13)$$

The time derivative of (12) and (13) is [21]

$$\dot{s}_k \cos\gamma_k - s_k\dot{\gamma}_k \sin\gamma_k = -\dot{\theta}_k \sin\theta_k + \dot{f}_{x,k} \quad (14)$$
$$\dot{s}_k \sin\gamma_k - s_k\dot{\gamma}_k \cos\gamma_k = \dot{\theta}_k \cos\theta_k + \dot{f}_{y,k}, \quad (15)$$

where $\dot{f}_{i,k} = \frac{\partial f_{i,k}}{\partial x_k}\dot{x}_k + \frac{\partial f_{i,k}}{\partial y_k}\dot{y}_k$. Solving for $\dot{s}_k$ in (14) and substituting the result into (15) to solve for $\dot{\gamma}_k$ yields [21]

$$\begin{aligned}\dot{\gamma}_k &= (1 - s_k^{-1}(f_{x,k}\cos\gamma_k + f_{y,k}\sin\gamma_k))u_k \\ &\quad + (\dot{f}_{y,k}\cos\gamma_k - \dot{f}_{x,k}\sin\gamma_k) \triangleq \nu_k,\end{aligned} \quad (16)$$

where ν_k is the steering control of the orientation of the total velocity. From (12), (13), and (16) we achieve the equations of motion for the k^{th} particle in a flowfield subject to steering control ν_k [21]:

$$\begin{aligned}\dot{x}_k &= s_k\cos\gamma_k \\ \dot{y}_k &= s_k\sin\gamma_k \\ \dot{\gamma}_k &= \nu_k,\ k = 1,\ldots,N.\end{aligned} \quad (17)$$

In a moderate flow, the transformation from ν_k to u_k (16) is nonsingular and the speed is [21]

$$\begin{aligned}s_k &= f_{x,k}\cos\gamma_k + f_{y,k}\sin\gamma_k \\ &\quad + \sqrt{1 - (f_{y,k}\cos\gamma_k - f_{x,k}\sin\gamma_k)^2}.\end{aligned} \quad (18)$$

The extension to a strong flowfield, i.e., one in which the flow magnitude can exceed the particle speed, is possible [27] but outside the scope of this paper where we assume a moderate flow.

B. Unobservability Measures

In linear systems theory, the singular values σ_j of the observability gramian determine the relative ease in determining the initial states of a linear system from the outputs generated over a time interval [28, p. 125-126]. Large singular values imply that it is easy to invert the mapping from outputs to initial states [9]. The reciprocal of the smallest singular value σ_{min} of the observability gramian, called the unobservability index, is a measure of the relative ease in which an estimation scheme can determine the initial state of a system [9]; large values imply that the system is difficult to observe, whereas small values indicate the opposite. The unobservability index is [9]

$$\xi \triangleq 1/\sigma_{min}. \quad (19)$$

In stochastic estimation, a large value of ξ implies that noise in the measurements will significantly impact the estimate error. Conversely, a small value of ξ implies that the estimation error may not be susceptible to measurement noise [9].

While the unobservability index is used to evaluate candidate sampling trajectories in this work, it is one of many metrics providing a measure of observability. For instance, the estimation condition number [7], [9]

$$\lambda = \frac{\sigma_{max}}{\sigma_{min}} = \sigma_{max}\xi, \quad (20)$$

reflects the degree of variability in the observability of the system. A large λ implies that a small perturbation in one direction may have a more pronounced effect on the output than a large perturbation in another direction, which implies that the observability of the system is sensitive to the perturbation direction and the estimation problem may be ill-conditioned [9]. Other metrics of the observability gramian include the trace, maximum singular value, and determinant [7], [20]. In this paper we choose the unobservability index (19) since it measures the least observable state.

Using the observability gramian on a nonlinear system to compute the unobservability index and the estimation condition number requires linearization about an equilibrium point. However, linearization may not adequately capture the input-output behavior of the nonlinear system over a desired operating region. Moreover, nonlinear observability analysis [18], [29] can be difficult to apply. One alternative for determining the observability of a nonlinear system is to use the empirical observability gramian [9], also known as the observability covariance matrix [10],[30]. The empirical observability gramian is useful because it approximates the input-output behavior of a nonlinear system and is equivalent to the observability gramian for a linear system.

The empirical observability gramian maps the input-to-state and state-to-output behavior of a nonlinear system more accurately than the observability gramian found by linearization [30]. It is

defined as follows. Let $\varepsilon_i \mathbf{e}_i$ be a small displacement of the initial parameter along the i^{th} unit vector $\mathbf{e}_i \in \mathbb{R}^M$ and let $\mathbf{\Omega} \in \mathbb{R}^M$ be the initial parameter state. The $(i,j)^{\text{th}}$ component of the $M \times M$ empirical observability gramian W_O is [9]

$$\begin{aligned} W_O(i,j) &= \frac{1}{4\varepsilon_i \varepsilon_j} \int_0^T \left[\boldsymbol{\alpha}^{+i}(\tau) - \boldsymbol{\alpha}^{-i}(\tau)\right]^T \\ &\quad \left[\boldsymbol{\alpha}^{+j}(\tau) - \boldsymbol{\alpha}^{-j}(\tau)\right] \mathrm{d}\tau, \\ &\quad i = 1,\ldots,M,\ j = 1,\ldots,M, \end{aligned} \tag{21}$$

where $\mathbf{\Omega}^{\pm i} = \mathbf{\Omega} \pm \varepsilon_i \mathbf{e}_i$, produces the output $\boldsymbol{\alpha}^{\pm i} = h(\mathbf{z}, \mathbf{u}; \mathbf{\Omega}^{\pm \mathbf{i}})$. Measures of the observability of a nonlinear system can be obtained by applying (19) and (20) to W_O.

Returning to the Rankine vortex example, assume each vehicle collects a (noise-free) flow measurement

$$\boldsymbol{\alpha}_k = [f_{x,k}, f_{y,k}]^T = \vec{f}_k \in \mathbb{R}^2. \tag{22}$$

such that $\boldsymbol{\alpha} = [\boldsymbol{\alpha}_1^T, \boldsymbol{\alpha}_2^T, \ldots, \boldsymbol{\alpha}_N^T]^T \in \mathbb{R}^{2N}$. The equations of motion in (1) with $\boldsymbol{\alpha}$ given by (22) produce a nonlinear input-output system.

Calculating the empirical observability gramian via integration of (1) with $g(\cdot)$ given by (17) reveals the input-output observability of the flowfield parameters $\mathbf{\Omega}$ over a given particle trajectory. The steering control input v_k dictates the sampling trajectory and is designed to stabilize optimal sampling trajectories. The perturbation size is chosen to be a fixed percentage of the nominal state size. For example, a 20% perturbation for $r_{max} = 30$ is $\varepsilon_1 = 6$.

C. Bayesian Estimation of a Parameterized Flowfield

We adopt a nonlinear estimation scheme to enable each particle to estimate the unknown parameters of a model flowfield. These estimates are used by each particle to compute its steering control. In this section we describe a recursive Bayesian filter formulation for parameter estimation.

Estimation of a spatiotemporal flowfield $\vec{f}$ of the form (6) using noisy observations of the flow can be accomplished by assimilating the observations using a recursive Bayesian filter. For linear systems with Gaussian noise, the optimal Bayesian filter is the Kalman filter, whereas for nonlinear systems with nonlinear noise models, a common Bayesian filter is a particle filter [31]. In either case, the flow estimate is encapsulated in a state vector, which for example may contain the flow velocity $\vec{f}$ at each one of P grid points. An alternative we pursue is a state vector $\mathbf{\Omega}$ that contains only a set of $M \ll P$ parameters, from which the flowfield $\vec{f}$ can be reconstructed. For example, the model (6) is defined by the $M = 3$ parameters $\mathbf{\Omega} = (r_{max}, v_{max}, \mu)$, such that the flowfield at $\vec{r}_k$ is $\vec{f}_k(\mathbf{\Omega}) = \vec{f}(x_k, y_k; \mathbf{\Omega})$. This representation provides a significant reduction in computations, making it attractive for use in an optimal sampling scheme. Note this representation is only possible for a parameterized flowfield.

The discrete-time Bayesian formalism proceeds as follows [31]. As in (2), let $\hat{\mathbf{\Omega}}(t)$ denote the state estimate at time t, $\tilde{\boldsymbol{\alpha}}_k(t)$ denote the k^{th} vehicle's noisy observation at time t, and $\mathbf{A}_k(t) = \{\tilde{\boldsymbol{\alpha}}_k(1), \ldots, \tilde{\boldsymbol{\alpha}}_k(t)\}$ denote the set of observations up to time t. The posterior probability of the state $\hat{\mathbf{\Omega}}(t)$ given $\mathbf{A}_k(t)$ is

$$\begin{aligned} p(\hat{\mathbf{\Omega}}(t)|\mathbf{A}_k(t)) &= \beta\, p(\tilde{\boldsymbol{\alpha}}_k(t)|\mathbf{\Omega}(t)) \\ &\quad p(\hat{\mathbf{\Omega}}(t)|\mathbf{A}_k(t-\Delta t)), \end{aligned} \tag{23}$$

where the coefficient β is chosen so that $p(\hat{\mathbf{\Omega}}(t)|\mathbf{A}_k(t))$ has unit integral over the state space. The conditional probability $p(\tilde{\boldsymbol{\alpha}}_k(t)|\mathbf{\Omega}(t))$ is a likelihood function that represents the probability that the state $\mathbf{\Omega}(t)$ generated the observation $\tilde{\boldsymbol{\alpha}}_k(t)$. Note that $p(\hat{\mathbf{\Omega}}(0)|\mathbf{A}_k(0))$ is the prior probability, which we assume to be uniform in the absence of any information other than the parameter lower and upper bounds.

Returning to the Rankine vortex example, suppose the k^{th} particle obtains the following noisy measurement of the flow at time t and location r_k:

$$\tilde{\boldsymbol{\alpha}}_k(t) = [f_{x,k}, f_{y,k}]^T + [\eta_{x,k}(t), \eta_{y,k}(t)]^T \in \mathbb{R}^2,$$

where the noise $\eta_{i,k}(t) \sim \mathcal{N}(0, \sigma_i^2)$ is normally distributed with zero mean and variance σ_i^2 for $i = x, y$. For each point $\mathbf{\Omega}(t)$ in the M-dimensional state space, we choose the likelihood function to be a multi-variate Gaussian, i.e.,

$$\begin{aligned} p(\tilde{\boldsymbol{\alpha}}_k(t)|\mathbf{\Omega}(t)) = \frac{1}{2\pi} \exp[&\frac{-1}{2}[\vec{f}_k(\mathbf{\Omega}(t)) - \tilde{\boldsymbol{\alpha}}_k(t)]^T \\ &\Sigma^{-1}[\vec{f}_k(\mathbf{\Omega}(t)) - \tilde{\boldsymbol{\alpha}}_k(t)]], \end{aligned} \tag{24}$$

where $\Sigma = \mathrm{diag}(\sigma_x^2, \sigma_y^2)$.

Assuming measurements are taken at each time step, the conditional probability density of the state

$\hat{\mathbf{\Omega}}(t)$ is updated with the equations of motion of the k^{th} particle in an Euler integration scheme such that the dynamics in (2) take the discrete form

$$p(\hat{\mathbf{\Omega}}(t)|\mathbf{A}(t)) = \beta\left(\prod_{k=1}^{N} p(\tilde{\boldsymbol{\alpha}}_k(t)|\mathbf{\Omega}(t))\right) p(\hat{\mathbf{\Omega}}(t)|\mathbf{A}(t-\Delta t)), \quad (25)$$

where $p(\tilde{\boldsymbol{\alpha}}_k(t)|\mathbf{\Omega}(t))$ is given by (24) and $p(\hat{\mathbf{\Omega}}(t)|\boldsymbol{A}(t-\Delta t))$ is the prior probability. We take the point in parameter space corresponding to the maximum of the posterior probability density $p(\hat{\mathbf{\Omega}}(t)|\mathbf{A}(t))$ to be the best estimate of the flowfield parameters $\hat{\mathbf{\Omega}}$. Note that (25) assumes that the k^{th} particle communicates its measurement to either a central hub or to every other particle such that all vehicles have knowledge of $p(\hat{\mathbf{\Omega}}(t)|\mathbf{A}(t))$. Distributed versions of (25) are possible [14], but beyond the scope of this paper.

III. Decentralized Multi-vehicle Control and Observability-based Sampling

In this section we derive controllers to stabilize multi-vehicle sampling trajectories that optimize the observability of a parameterized flowfield. Sampling trajectories are chosen from a family of sampling formations parameterized by $\boldsymbol{\chi}$. For example, the family of circular sampling patterns is parameterized by the position of the circle's center and its radius. For flowfields with azimuthal symmetry such as a Rankine vortex model (7)–(8), the azimuth of the circular pattern's center is irrelevant and the family of circular formations is parameterized by the distance ρ of the center from the origin and the radius of the circle $|\omega_0|^{-1}$. This section presents a decentralized multi-vehicle control algorithm to steer vehicles to circular formations parameterized by $\boldsymbol{\chi} = (\rho, |\omega_0|^{-1})$. The empirical observability gramian is used to evaluate the family of candidate sampling trajectories and an observability-based algorithm is presented to steer vehicles to optimal sampling formations.

A. Stabilization of Circular Formations with Arbitrary Azimuth

This subsection uses Lyapunov-based control techniques [32] to derive a decentralized control algorithm that steers vehicles to a circular formation parameterized by $\boldsymbol{\chi} = (\rho, |\omega_0|^{-1})$. The control laws are derived assuming the particles travel through a known, time-invariant flowfield. We relax the known-flowfield assumption in Section IV, using instead flowfield estimates provided by a recursive Bayesian filter.

A particle traveling in a circle rotates about a fixed point in space. Let the instantaneous circle center [21], [22] be defined by

$$\vec{c}_k = \vec{r}_k + (\omega_0 s_k)^{-1}[-\dot{y}_k, \dot{x}_k]^T = [c_{x,k}, c_{y,k}]^T \in \mathbb{R}^2, \quad (26)$$

where $|\omega_0|^{-1}$ is the radius of the circle. From the time derivative of (26),

$$\dot{\vec{c}}_k = \dot{\vec{r}}_k(1 - (\omega_0 s_k)^{-1} \nu_k), \quad (27)$$

we see that $\dot{\vec{c}}_k = 0$ for the control $\nu_k = \omega_0 s_k$, which steers the k^{th} particle about a fixed center $\vec{c}_k = \vec{c}_k(0)$. The following control law forces the k^{th} particle to converge to a circular trajectory in which the steady-state value $||\vec{c}_k|| = \rho$ is specified.

Theorem 1: The particle model (17) with control

$$\nu_k = \omega_0 s_k[1 + K(\dot{\vec{r}}_k^T \vec{r}_k)(1 - \rho||\vec{c}_k||^{-1})], \quad K > 0, \quad (28)$$

stabilizes the set of circular trajectories with radius $|\omega_0|^{-1}$ centered at distance ρ from the origin of reference frame $\mathscr{I}$.

Proof: Consider the potential function

$$V = \sum_{k=1}^{N} \frac{1}{2}(||\vec{c}_k|| - \rho)^2, \quad (29)$$

where $||\vec{c}_k|| = \sqrt{\vec{c}_k^T \vec{c}_k}$ is the distance of circle center k from origin O. The time derivative of (29) along solutions to the equations of motion (17) is

$$\dot{V} = \sum_{k=1}^{N} (1 - \rho||\vec{c}_k||^{-1})(\dot{\vec{r}}_k^T \vec{r}_k)(1 - (\omega_0 s_k)^{-1} \nu_k). \quad (30)$$

Substituting the control (28) into (30) gives

$$\dot{V} = -K \sum_{k=1}^{N} [\dot{\vec{r}}_k^T \vec{r}_k (1 - \rho||\vec{c}_k||^{-1})]^2 \leq 0. \quad (31)$$

Equation (31) implies that $\dot{V}$ is negative semi-definite with $\dot{V} = 0$ occurring when $||\vec{c}_k|| = \rho$ or $\dot{\vec{r}}_k^T \vec{r}_k = 0$ for all k, which occurs when $||\vec{c}_k|| = 0$ since $\dot{\vec{r}}_k \neq 0$. The largest invariant set Λ for

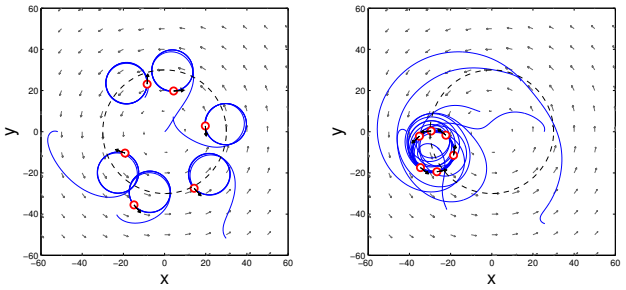

(a) (b)

Fig. 2. Simulation of $N = 6$ particles in a Rankine vortex with (a) control algorithm (28) and (b) steering control algorithm (33).

which $\dot{V} = 0$ contains circular trajectories with $||\vec{c}_k|| = \rho$ or $||\vec{c}_k|| = 0$. The invariance principle [32] stipulates that particle k converges to Λ. ■

Figure 2(a) shows a simulation of the control law (28) with $N = 6$ particles in a Rankine vortex described by (7)–(8) with $r_{max} = 30$, $v_{max} = 0.7$, and $\mu = 0.6$. Note that each particle converges to a circular trajectory of radius $|\omega_0|^{-1} = 10$ whose center lies on the dashed line corresponding to $\rho = 30$. The control gain is $K = 0.1$.

To guarantee particle convergence to a single circular formation whose center is a desired distance from the origin, we utilize a composite potential. Let $\vec{\mathbf{c}} = [\vec{c}_1, \vec{c}_2, \ldots, \vec{c}_N]^T \in \mathbb{R}^{N\times 2}$. Consider the potential

$$V = \frac{1}{2}\sum_{k=1}^{N}\left[\vec{c}_k^T(\mathbf{P}_k\vec{\mathbf{c}})^T + a_{k0}(||c_k|| - \rho)^2\right], \quad (32)$$

where $a_{k0} = 1$ if the k^{th} particle is informed of ρ and zero otherwise and $\mathbf{P}_k$ is the k^{th} row of the $N\times N$ projection matrix $\mathbf{P} = I_{N\times N} - (1/N)\mathbf{1}\mathbf{1}^T$. We have the following result.

Theorem 2: The particle model (17) with control

$$\begin{aligned} v_k &= \omega_0 s_k(1 + K[\dot{\vec{r}}_k^T(\mathbf{P}_k\vec{\mathbf{c}})^T \\ &\quad + a_{k0}(1-\rho||\vec{c}_k||^{-1})\dot{\vec{r}}_k^T\vec{r}_k]) \end{aligned} \quad (33)$$

stabilizes the set of circular formations with radius $|\omega_0|^{-1}$ whose center is ρ units from the origin.

Proof: The time derivative of (32) along solutions of (17) is

$$\begin{aligned} \dot{V} = \sum_{k=1}^{N}&\left[\dot{\vec{r}}_k^T(\mathbf{P}_k\vec{\mathbf{c}})^T + a_{k0}(1-\rho||\vec{c}_k||^{-1})\dot{\vec{r}}_k^T\vec{r}_k\right] \\ &(1-(\omega_0 s_k)^{-1}v_k). \end{aligned} \quad (34)$$

Substituting (33) into (34) gives $\dot{V} \le 0$ since

$$\dot{V} = -K\sum_{k=1}^{N}\left[\dot{\vec{r}}_k^T(\mathbf{P}_k\vec{\mathbf{c}})^T + a_{k0}(1-\rho||\vec{c}_k||^{-1})\dot{\vec{r}}_k^T\vec{r}_k\right]^2. \quad (35)$$

Equation (35) implies that the vehicles converge to the largest invariant set Λ for which

$$\dot{\vec{r}}_k^T(\mathbf{P}_k\vec{\mathbf{c}})^T + a_{k0}(1-\rho||\vec{c}_k||^{-1})\dot{\vec{r}}_k^T\vec{r}_k \equiv 0. \quad (36)$$

Since $||\dot{\vec{r}}_k|| \neq 0$, (36) is satisfied only when $\mathbf{P}_k\vec{\mathbf{c}} = 0$ and $||\vec{c}_k|| = \rho$. The quantity $\mathbf{P}_k\vec{\mathbf{c}} = 0$ only when $\vec{c}_k = \vec{c}_j$ for all pairs j,k [22]. By the invariance principle [32] solutions converge to Λ, which contains the desired set of circular formations. ■

Simulation of the control algorithm (33) with $N = 6$ particles in a Rankine vortex is shown in Figure 2(b) with $|\omega_0|^{-1} = 10$, $K = 0.1$, $a_{1,0} = a_{2,0} = a_{3,0} = 1$, and $a_{4,0} = a_{5,0} = a_{6,0} = 0$. The particles converge to a circular formation with distance $\rho = 30$ from the origin, shown by the dashed line.

B. Observability-based Optimization of Control Parameters

In this section we present an algorithm that uses nonlinear observability to optimize the parametric inputs to a coordinated sampling formation. In many environmental sampling applications, vehicles are driven in repeating patterns to collect measurements within a spatiotemporal volume [33]. The control algorithms driving vehicles to these formations require a set of parameter inputs $\boldsymbol{\chi}$, such as $\boldsymbol{\chi} = (\rho, |\omega_0|^{-1})$ for the circular formations in Section III-A. Here we use the unobservability index (19) as a metric to evaluate the ability of members of the formation parameter space $\boldsymbol{\chi}$ to observe a flowfield parameterized by $\boldsymbol{\Omega}$.

In a known flowfield, a set of sampling parameters $\boldsymbol{\chi}$ produces a corresponding unobservability index $\xi(\boldsymbol{\chi})$ calculated from (1), (19), and (21). The optimal trajectory is found by optimizing over the space of sampling parameters

$$\boldsymbol{\chi}^* = \text{argmin } \xi(\boldsymbol{\chi}). \quad (37)$$

Since this optimization technique iterates only over the low-dimensional sampling parameter space, rather than the space of all possible sampling trajectories, it can be computed rapidly even by an exhaustive search.

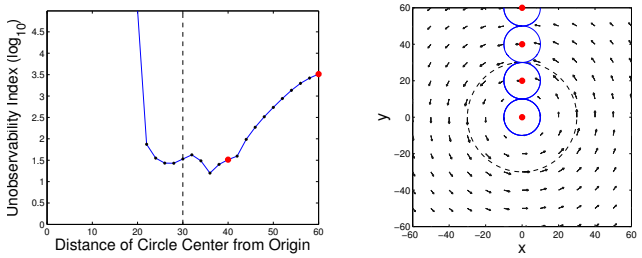

(a) (b)

Fig. 3. (a) Unobservability index versus distance of circular sampling formation from vortex origin. (b) A sample of controlled trajectories. The red circle centers at $y = 40$ and $y = 60$ correspond to the red data points of (a).

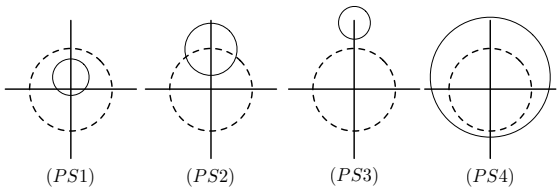

Fig. 4. Pattern subsets associated with a circular sampling formation in a Rankine vortex. The dotted line represents r_{max}.

Figure 3 shows analysis of circular trajectory optimization in a Rankine vortex (7)–(8) parameterized by the flowfield parameters $\mathbf{\Omega} = (r_{max}, v_{max}, \mu)$. The sampling parameter space $\boldsymbol{\chi} = (\rho, 10)$ is the set of circular formation center distances ρ from the origin, assuming circular formations of radius $|\omega_0|^{-1} = 10$. Figure 3(a) shows the log of the unobservability index as a function of the sampling parameter ρ. Figure 3(b) shows four sampling trajectories corresponding to the red data points of Figure 3(a). In each case, the initial position of the vehicle is located on the desired circle to eliminate the effect of transient behavior on the unobservability analysis. The flowfield parameters are $\mathbf{\Omega} = (30, 0.7, 0.6)$. r_{max} is shown by the dashed line in both figures. Notice that the unobservability is minimized by traveling in a circle with $\rho^* = 35$. For $\rho < 20 = r_{max} - |\omega_0|^{-1}$ there is an increase in unobservability because the flowfield parameter μ, corresponding to the decay in flowspeed outside of r_{max}, is unobservable. For $\rho > 40$ the parameters are less observable because the flow strength decreases exponentially outside the radius of maximum wind.

Figure 4 shows four pattern subsets of the sampling parameter space that provide significantly different observability. Pattern subset #1 ($PS1$) contains circular trajectories that lie entirely inside r_{max}. $PS2$ trajectories cross r_{max}. $PS3$ lies entirely outside r_{max} with $|\omega_0|^{-1} < r_{max}$. $PS4$ contains r_{max}. Since the Rankine vortex model is azimuthally symmetric, the circle centers are constrained to the y-axis without loss of generality.

Figure 5 shows the results of unobservability analysis over $\boldsymbol{\chi} = (\rho, |\omega_0|^{-1})$, in which the parameter-space boundaries of the pattern subsets are evident. Figure 5(a) depicts example trajectories from within each subset as well as the subset boundaries, which are found analytically. Figure 5(b) shows the unobservability index over the parameter space. In both figures ρ and $|\omega_0|^{-1}$ are normalized by r_{max}. Note that areas of low unobservability correspond to trajectories crossing r_{max} ($PS2$), whereas highly unobservable trajectories remain entirely inside ($PS1$) or outside ($PS4$) r_{max}. Trajectories in pattern subset ($PS3$) are less observable than ($PS2$), but more observable than ($PS1$) and ($PS4$). The minimum of the unobservability index is shown by the white dot in Figure 5(b), along with a scaled image of the optimal trajectory.

IV. Observability-based Sampling in an Estimated Flowfield

In this section we combine the results of Sections II and III in an optimal sampling algorithm and provide a numerical example of vehicles sampling in a Rankine vortex. A recursive Bayesian filter estimates the flowfield parameters, which are utilized to determine optimal sampling parameters over a time interval T_{opt}. The multi-vehicle control algorithm (33) is implemented using the flowfield estimate and the optimal sampling parameters, such that vehicles are steered to trajectories with optimal observability.

The sampling algorithm proceeds as follows. First, the probability density function for the flowfield parameters $\mathbf{\Omega}$ is initialized either uniformly within known bounds or from a known prior distribution. The maximum of the probability density function corresponds to the initial flowfield parameters $\hat{\mathbf{\Omega}}(0)$ upon which the initial flowfield estimate $\hat{f}_k = f(x_k, y_k; \hat{\mathbf{\Omega}}(0))$ is based. The initial estimate is utilized in (22) to calculate $W_O(\boldsymbol{\chi})$ using (21)

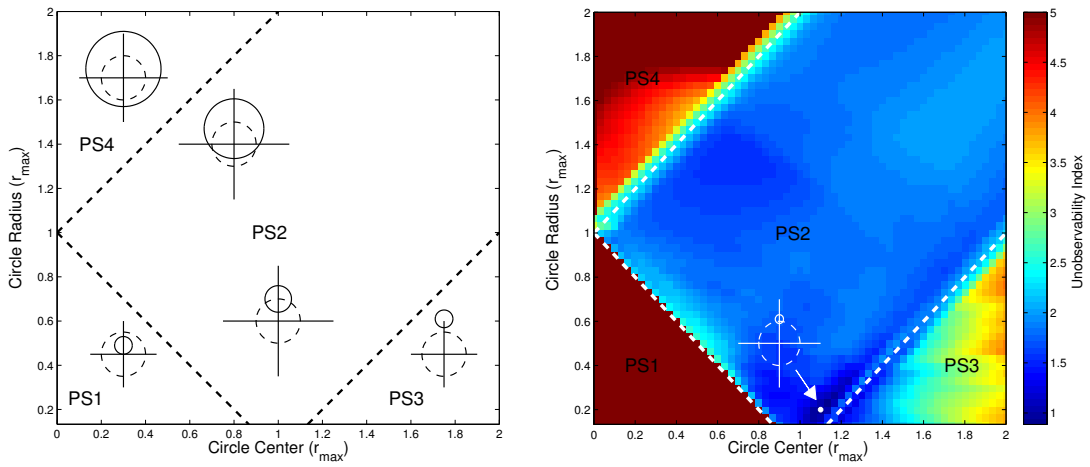

(a) (b)

Fig. 5. Observability of a Rankine vortex. (a) Pattern subsets over the parameter space $\boldsymbol{\chi} = (\rho, |\omega_0|^{-1})$ normalized by r_{max}. (b) The unobservability index $\xi(\boldsymbol{\chi})$ with minimum denoted by the white dot.

over a time horizon T_{opt} and sampling parameters $\boldsymbol{\chi}$. (Note that in this step the transient behavior of the vehicles as they converge to the formation $\boldsymbol{\chi}$ is taken into account; the initial positions of each particle are used to calculate (21).) The choice of horizon time depends on the expected accuracy of the flowfield estimate. For instance, one may choose T_{opt} to be relatively short initially since the vehicles have yet to collect measurements. In this work, we assume a constant horizon time of $T_{opt} = 50$ seconds.

The optimal sampling parameters $\boldsymbol{\chi}^*$ over T_{opt} found using (37) are implemented in the control algorithm $\nu_k = \nu_k(x_k, y_k, \hat{\vec{f}}_k; \boldsymbol{\chi}^*)$, where ν_k is given by (33). Particles travel along the closed-loop trajectories, collecting noisy measurements $\tilde{\boldsymbol{\alpha}}_k(t)$ and using the flowfield estimates $\hat{\vec{f}}_k = f(x_k, y_k; \hat{\boldsymbol{\Omega}}(t))$ in the decentralized control. After time T_{opt} has elapsed, the process is repeated on T_{opt} intervals to produce an updated set of optimal sampling parameters $\boldsymbol{\chi}^*$ from the new flowfield parameters $\hat{\boldsymbol{\Omega}}(t)$ until the mission completes. An overview of the sampling algorithm is shown in Table 1 with an associated block diagram shown in Figure 6.

We simulated the observability-based sampling algorithm with $N = 5$ vehicles to estimate the flowfield parameters $\boldsymbol{\Omega} = (r_{max}, v_{max}, \mu)$ of the Rankine vortex model (7)–(8). The initial vehicle positions were clustered outside r_{max} and the flowfield was assumed to have ground-truth parameters $r_{max} =$ 30, $v_{max} = 0.5$, and $\mu = 0.8$. The duration of the sampling mission was 400 seconds with observability iteration occurring every $T_{opt} = 50$ seconds. The probability density function was initialized uniformly over the parameter space $r_{max} \in [0, 100]$, $v_{max} \in [0.01, 1]$, and $\mu \in [0, 1]$, and the initial flowfield parameter estimate was selected randomly within the space. For simplicity we assumed the radius of the desired circular formation was held

Table 1 Observability-based Sampling Algorithm.

Inputs: probability density $p(\hat{\boldsymbol{\Omega}}(t)|\tilde{\boldsymbol{\alpha}}(0))$ producing initial flowfield estimate $\hat{\boldsymbol{\Omega}}(0)$; $\boldsymbol{\chi}(0)^* = \text{argmin } \xi(\boldsymbol{\chi}; \hat{\boldsymbol{\Omega}}(0), T_{opt})$ using observability analysis and initial vehicle positions over iteration time T_{opt}; T_{final}; T_{opt}.

for $t < T_{final}$ **do**

1. Generate an estimated flowfield using estimated parameters, $\hat{\vec{f}}_k(t) = \vec{f}(x_k(t), y_k(t); \hat{\boldsymbol{\Omega}}(t))$.
2. Use the estimated flowfield and the current optimal sampling parameters to calculate the steering control $\nu_k(t) = \nu(\boldsymbol{x}(t), \boldsymbol{y}(t), \hat{\vec{f}}(t); \boldsymbol{\chi}^*)$.
3. Update the flowfield parameter estimate by assimilating measurements, so that $\hat{\boldsymbol{\Omega}}(t) = \sup p(\hat{\boldsymbol{\Omega}}(t)|\mathbf{A}(t))$.

if $t \mod T_{opt} = 0$ **then**

Find the optimal sampling parameters over the observability iteration time using the current particle positions and current flowfield parameter estimate, $\boldsymbol{\chi}^* = \text{argmin}\xi(\boldsymbol{\chi}; \hat{\boldsymbol{\Omega}}(t), T_{opt})$.

end if

4. Set $t = t + \Delta t$

end for

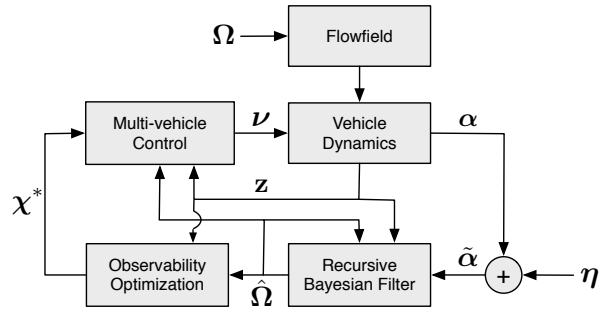

Fig. 6. A schematic diagram of the observability-based sampling algorithm is shown. A recursive Bayesian filter provides flowfield parameter estimates $\hat{\boldsymbol{\Omega}}$ from noisy flow measurements $\tilde{\boldsymbol{\alpha}}$. The estimated flowfield parameters are used to calculate observability optimizing control parameters $\boldsymbol{\chi}^*$ that characterize the multi-vehicle sampling formation.

constant at $|\omega_0|^{-1} = 10$ so the observability analysis takes place over the sampling parameter space $\boldsymbol{\chi} = (\rho, 10)$.

Figure 7 shows a snapshot of the sampling algorithm simulation at $t = 20$ seconds. Figures 7(a) and 7(b) show the log of two marginal probability densities[2] over the flowfield parameter space r_{max}, v_{max}, and μ. In each figure the black dot corresponds to the ground truth parameters and the magenta dot corresponds to the current estimate. Figure 7(c) shows the result of the initial unobservability analysis. The red dot corresponds to the sampling parameter with the highest observability; the black and magenta dashed lines correspond to the true and estimated r_{max} values, respectively. Figure 7(d) shows the position and velocity orientation of each particle after $t = 20$ seconds. The black and magenta dashed circles correspond to the ground truth and estimated r_{max} values, respectively. The true flowfield is plotted in black while the estimated flowfield is shown in grey. The red circle corresponds to the optimal circle center distance ρ^*.

Figure 8 shows a snapshot of the sampling mission at $t = 400$ seconds. Figure 8(d) shows the full particle trajectory in light blue while the converged formation is in dark blue. Notice that the mode of the posterior of the Bayesian filter has converged to the ground-truth. The unobservability analysis in Figure 8(c) agrees with the predictions in Figure 5(b) in the following sense: for fixed circle radius $|\omega_0|^{-1} = 10$ corresponding to $|\omega_0|^{-1}/r_{max} = 0.33$, the optimal circular formation has center distance $\rho/r_{max} = 0.85$, corresponding to the minimum of Figure 5(b) for that circle radius.

[2]The marginal probability density is the sum of a multi-dimensional probability density function over a single dimension.

V. CONCLUSION

This paper presents a multi-vehicle sampling algorithm that maximizes the observability of an estimated flowfield. The sampling algorithm steers vehicles to optimal sampling trajectories selected from a parameterized space of candidate sampling trajectories. The observability of the parameters defining a flowfield model is evaluated along candidate trajectories using the empirical observability gramian. The optimal flowfield observability is achieved by minimizing the unobservability index, which is the reciprocal of the smallest singular value of the empirical observability gramian. We employ a recursive Bayesian filter to provide estimates of the flow to the steering control algorithm. Numerical simulations of the algorithm in a Rankine vortex suggest that the sampling algorithm estimates the flowfield parameters even when noisy measurements of the flow are used. In ongoing research we are expanding this sampling algorithm to higher fidelity flowfield and vehicle models, including flowfields in which vehicles may not be able to maintain forward progress against the flow.

VI. ACKNOWLEDGMENTS

The authors would like to acknowledge Kayo Ide, Sean Humbert, Doug Koch, and Angela Maki for discussions related to this work.

REFERENCES

[1] J. Elston, B. Argrow, E. Frew, and A. Houston, "Evaluation of UAS concepts of operation for severe storm penetration using hardware-in-the-loop simulations," in *AIAA Guidance, Navigation, and Control Conference*, Toronto, Canada, August 2010, pp. 8178–8193.

[2] N. Leonard, D. A. Paley, F. Lekien, R. Sepulchre, D. Fratantoni, and R. Davis, "Collective motion, sensor networks, and ocean sampling," *Proceedings of the IEEE*, vol. 95, no. 1, pp. 48–74, 2007.

[3] P. Lin, "Observations: The first successful typhoon eyewall-penetration reconnaissance flight mission conducted by the unmanned aerial vehicle, Aerosonde," *Bulletin of the American Meteorological Society*, vol. 87, pp. 1481–1483, 2006.

[4] "Hurricane basics," National Oceanographic and Atmospheric Administration (NOAA), http://hurricanes.noaa.gov/pdf/hurricanebook.pdf, May 1999.

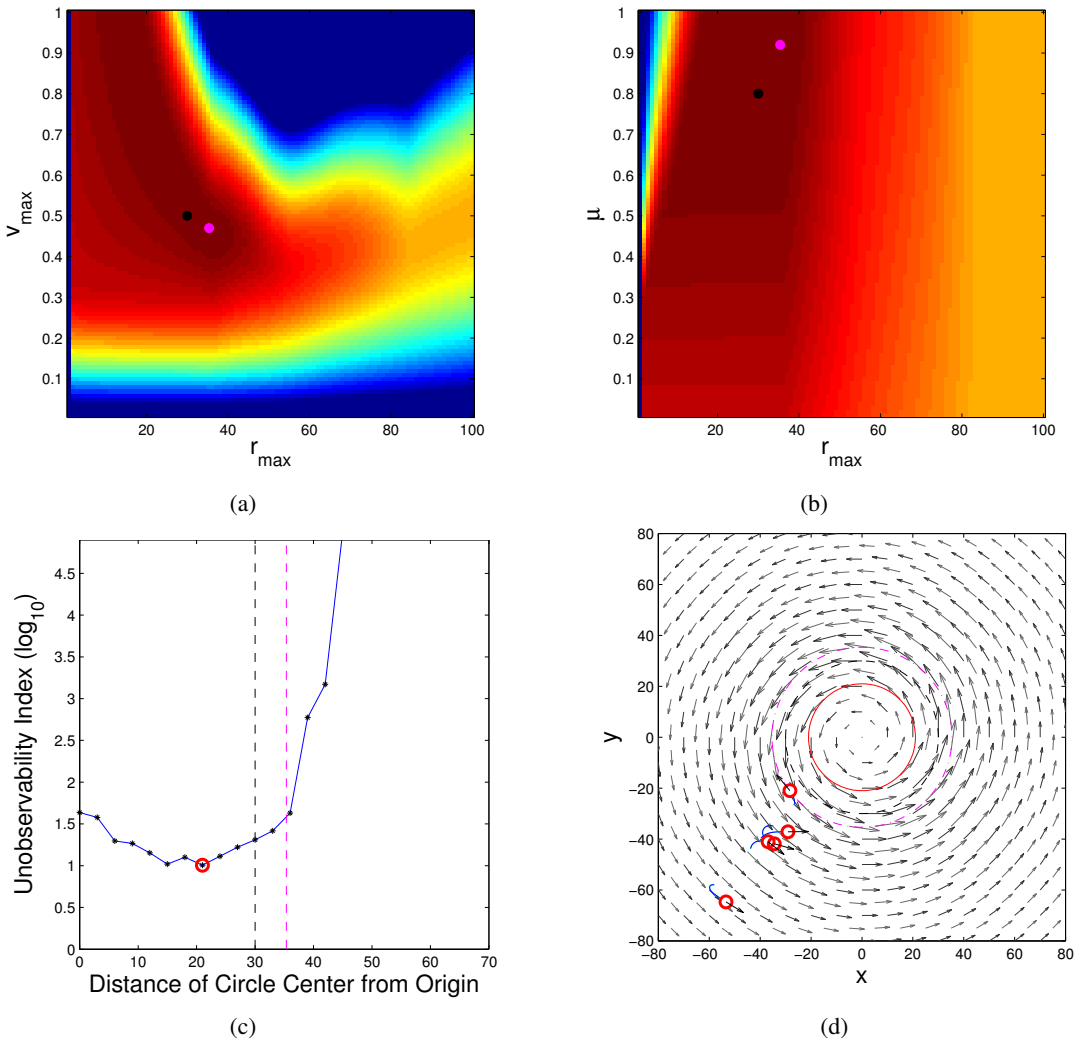

Fig. 7. Snapshot of the observability-based sampling algorithm at $t = 20$ seconds. (a)–(b) The log of marginal probability densities over the parameter space $\mathbf{\Omega}$. (c) The unobservability index versus ρ with the minimum shown by the red data point. (d) Particle trajectories are shown in a Rankine vortex with the desired circle center radius ρ shown by the red circle.

[5] A. J. Krener, "Eulerian and lagrangian observability of point vortex flows," *Tellus*, vol. 60, pp. 1089–1102, 2008.

[6] J. Cortes, S. Martinez, T. Karatas, and F. Bullo, "Coverage control for mobile sensing networks," *IEEE Transactions on Robotics and Automation*, vol. 20, no. 2, pp. 243–255, April 2004.

[7] A. K. Singh and J. Hahn, "Determining optimal sensor locations for state and parameter estimation for stable nonlinear systems," *Industrial and Engineering Chemistry Research*, vol. 44, no. 15, pp. 5645–5659, June 2005.

[8] N. R. Lawrance and S. Sukkarieh, "Autonomous exploration of a wind field with a gliding aircraft," *Journal of Guidance, Control, and Dynamics*, vol. 34, no. 3, pp. 719–733, May-June 2011.

[9] A. Krener and K. Ide, "Measures of unobservability," in *IEEE Conference on Decision and Control*, Shanghai, China, December 2009, pp. 6401–6406.

[10] S. Lall, J. Marsden, and S. A. Glavaski, "A subspace approach to balanced truncation for model reduction of nonlinear control systems," *International Journal of Robust and Nonlinear Control*, vol. 12, no. 6, pp. 519–535, 2002.

[11] M. A. Demetriou, "Guidance of mobile actuator-plus-sensor networks for improved control and estimation of distributed parameter systems," *IEEE Transactions on Automatic Control*, vol. 55, no. 7, pp. 1570–1584, July 2010.

[12] Z. Song, Y. Chen, J. Liang, and D. Ucinski, "Optimal mobile sensor motion planning under nonholonomic constraints for parameter estimation of distributed systems," in *In Proc. of IEEE International Conference on Intelligent Robots and Systems*, Edmonton, Alberta, Canada, August 2005, pp. 3163–3168.

[13] H. Chao and Y. Chen, "Surface wind profile measurement using multiple small unmanned aerial vehicles," in *In Proc. of the 2010 American Control Conference*, June-July 2010, pp. 4133–4138.

[14] K. M. Lynch, I. B. Schwartz, P. Yang, and R. A. Freeman, "Decentralized environmental modeling by mobile sensor networks," *IEEE Transactions on Robotics*, vol. 24, no. 3, pp. 710–724, 2008.

[15] H. J. Palanthandalam-Madapusi, A. Girard, and D. S. Bern-

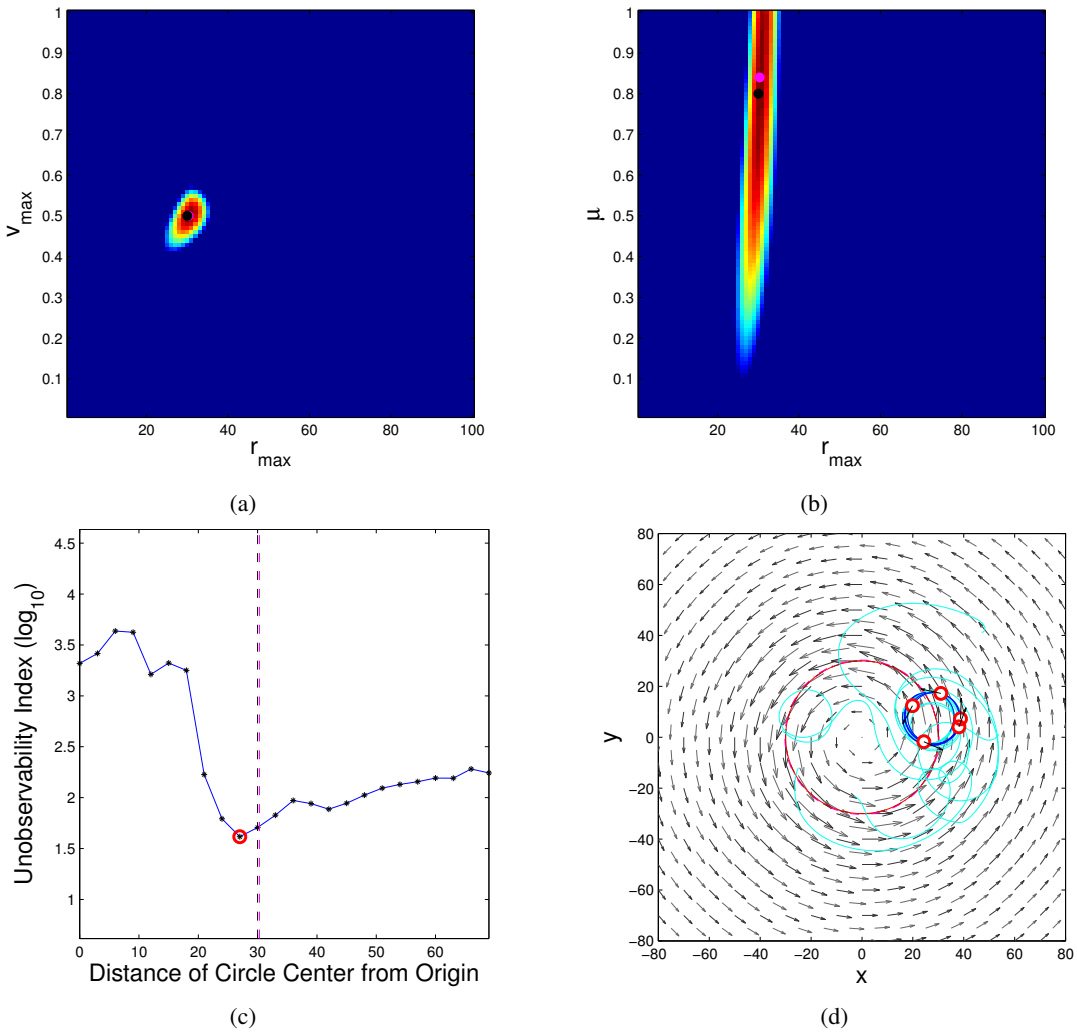

Fig. 8. Snapshot of the observability-based sampling algorithm at $t = 400$ seconds. (a)–(b) The log of marginal probability densities over the parameter space $\mathbf{\Omega}$. (c) The unobservability index versus ρ with the minimum shown by the red data point. (d) Particle trajectories are shown in light blue with the converged formation shown in dark blue.

stein, "Wind-field reconstruction using flight data," in *Proc. of the 2008 American Control Conference*, 2008, pp. 1863–1868.

[16] J. W. Langelaan, N. Alley, and J. Neidhoefer, "Wind field estimation for small unmanned aerial vehicles," *Journal of Guidance, Control, and Dynamics*, vol. 34, no. 4, pp. 1016–1030, July-August 2011.

[17] S. Mulgund and R. F. Stengel, "Optimal nonlinear estimation for aircraft flight control in wind shear," *Automatica*, vol. 32, no. 1, pp. 3–13, 1996.

[18] R. Hermann and A. J. Krener, "Nonlinear controllability and observability," *IEEE Transactions on Automatic Control*, vol. 22, no. 5, pp. 728–740, 1977.

[19] H. Salman, L. Kuznetsov, C. K. R. T. Jones, and K. Ide, "A method of assimilating Lagrangian data into a shallow-water-equation ocean model," *Monthly Weather Review*, vol. 134, pp. 1081–1101, April 2006.

[20] A. V. Wouwer, N. Point, S. Porteman, and M. Remy, "An approach to the selection of optimal sensor locations in distributed parameter systems," *Journal of Process Control*, vol. 10, no. 4, pp. 291–300, August 2000.

[21] D. A. Paley and C. Peterson, "Stabilization of collective motion in a time-invariant flowfield," *AIAA Journal of Guidance, Control, and Dynamics*, vol. 32, pp. 771–779, June 2009.

[22] R. Sepulchre, D. A. Paley, and N. E. Leonard, "Stabilization of planar collective motion: All-to-all communication," *IEEE Transactions on Automatic Control*, vol. 52, pp. 811–824, May 2007.

[23] L. Techy, D. A. Paley, and C. Woolsey, "UAV coordination on closed convex paths in wind," *AIAA Journal of Guidance, Control, and Dynamics*, vol. 33, pp. 1946–1951, 2010.

[24] L. Arranz, A. Seuret, and C. C. de Wit, "Contraction control of a fleet circular formation of AUVs under limited communication range," in *American Control Conference*, Baltimore, MD, June 2010, pp. 5991–5996.

[25] R. Sepulchre, D. A. Paley, and N. E. Leonard, "Stabilization of planar collective motion with limited communication," *IEEE Transactions on Automatic Control*, vol. 53, pp. 706–719, April 2008.

[26] N. L. R. Sepulchre, D. A. Paley, "Stabilization of collective motion of self-propelled particles," *Proc. 16th Int. Symp. Mathematical Theory of Networks and Systems*, p. 10, July

2004.

[27] L. DeVries and D. A. Paley, "Multi-vehicle control in a strong flowfield with application to hurricane sampling," *Journal of Guidance, Control, and Dynamics*, vol. 35, no. 3, pp. 794–806, May-June 2012.

[28] S. Skogestad and I. Postlethwaite, *Multivariable Feedback Control: Analysis and Design*. West Sussex, England: John Wiley and Sons, 1996.

[29] U. Vaidya, "Observability gramian for nonlinear systems," in *Proc. of the 46th IEEE Conf. on Decision and Control (CDC)*, New Orleans, LA, Dec. 2007, pp. 3357–3362.

[30] J. Hahn and T. F. Edgar, "A gramian based approach to nonlinear quantification and model classification," *Industrial and Engineering Chemistry Research*, vol. 40, pp. 5724–5731, 2001.

[31] N. Bergman, "Recursive Bayesian estimation navigation and tracking applications," Ph.D. dissertation, Department of Electrical Engineering, Linkoping University, Sweden, 1999.

[32] H. K. Khalil, *Nonlinear Systems*, 3rd ed. Prentice Hall, 2002.

[33] D. A. Paley, F. Zhang, and N. E. Leonard, "Cooperative control for ocean sampling: The Glider Coordinated Control System," *IEEE Transactions on Control Systems Technology*, vol. 16, no. 4, pp. 735–744, 2008.